Catalytic decomposition of methane into hydrogen and carbon nanotubes over mesostructured silica nanoparticle-supported nickel catalysts

Nur Shamimie Nadzwin Hasnan[1] · Sharifah Najiha Timmiati[1] · Manoj Pudukudy[2,3] · Zahira Yaakob[3] · Kean Long Lim[1] · Yun Hin Taufiq-Yap[4]

Abstract

Hydrogen is an alternative source of renewable energy that can be produced by methane decomposition without any CO_x formation. In this work, an impregnation method was used to prepare a set of Ni-based catalysts (5% to 50%) supported on mesostructured silica nanoparticles (MSNs) for its application in methane decomposition. The use of MSN as an effective support for nickel in methane decomposition was reported here for the first time. The physical, chemical and structural properties of the catalysts was studied and the results indicated that NiO was the active species in the fresh catalyst that were effectively distributed on the mesoporous surface of MSN. The reduction temperature of Ni/MSN catalysts were shifted to low temperatures with increased loading of nickel. The hydrogen yield increased with the increment of Ni amount in the catalysts. The catalytic activity of the 50% Ni/MSN catalyst showed that this catalyst was highly efficient and stable compared with other catalysts. The catalyst showed the highest hydrogen yield of 68% and remained more or less the same during 360 min of reaction. Approximately 62% of hydrogen yield was observed at the end of reaction. Further analysis on the spent catalysts confirmed that carbon nanotubes was formed over Ni/MSN catalyst with high graphitization degree.

Keywords Hydrogen production · Mesostructured silica nanoparticles · Ni/MSN catalysts · Carbon nanotubes · Surface catalysis

1 Introduction

The rapid development of human activities has led to global warming that has become a major concern worldwide. The reality of the alternative energy in the industrial sector is a transformation towards pollution, energy security and globalisation. In the early 1980s and 1990s, fuel cells were extensively known as a front-line technology that introduced hydrogen as an alternative energy, which is becoming a major component of renewable energy worldwide for stationary and transportation use, as well as electrical sources centred on buildings [1]. Fuel cell requires hydrogen for handling process, thereby resulting in the various technologies for hydrogen storage in its distribution for mobile applications. The potential use of hydrogen as a transport fuel is based on its thermal properties, and it can be compared with current fuel combustion, such as based on the combustion of gasoline and natural gas [2]. Hydrogen produces better efficiency and is more environmentally friendly than conventional petroleum-based fuels [3–5].

✉ Sharifah Najiha Timmiati
najiha@ukm.edu.my

✉ Manoj Pudukudy
manojpudukudy@gmail.com

1 Fuel Cell Institute, Universiti Kebangsaan Malaysia, 43600 Bangi, Selangor, Malaysia

2 Faculty of Chemical Engineering, Kunming University of Science and Technology, Kunming 650500, Yunnan, People's Republic of China

3 Research Centre for Sustainable Process Technology (CESPRO), Faculty of Engineering and Built Environment, Universiti Kebangsaan Malaysia, 43600 Bangi, Selangor, Malaysia

4 Catalysis Science and Technology Research Centre, Faculty of Science, Universiti Putra Malaysia, 43400 Serdang, Selangor, Malaysia

Hydrogen can be produced from a variety of sources, such as biomass, natural gas, water and hydrocarbons, by using various methods. Steam reforming is commonly used in hydrogen production from hydrocarbon, especially from methane, due to its abundant sources. However, the presence of CO and CO_2 as the by-products and coke formation that eventually causes catalyst deactivation are the major drawbacks of steam reforming [6–10]. Hence, methane decomposition is introduced as another possible method for hydrogen production from methane because it produces CO_x-free hydrogen and solid carbon with different morphologies as a product. The process is also simple, and no purification of products, such as in water–gas shift reaction, is required because the process does not produce any greenhouse gas as a by-product of the reaction [11–13]. The solid carbon produced may be in various carbon form depending on the catalyst used. Most of the ordered nanocarbon structure of the produced carbon can be obtained using a metal-based catalyst, while carbon-based catalyst generally results in amorphous carbon [14].

The methane decomposition is an endothermic process involving the use of high temperature to decompose methane because of the strong bond between C and H, which are very difficult to break. Therefore, the use of the catalyst can reduce the reaction temperature to break the C–H bond [15–17]. Hydrogen production through methane decomposition is an approach that has a considerable prospect and has been studied extensively. The natural properties of metal species, the thermal stability of catalyst supports and the surface area of the catalyst considerably influence the catalytic activity. The transition metals such as Ni, Fe, Cu and Co-based catalysts that are supported on various supports are commonly used in methane decomposition due to its low cost. Among the studied metal catalysts in methane decomposition, Ni is one the most effective catalysts and commercially available. The selection of a catalyst support helps in determining catalytic performance in terms of methane conversion and improving its stability for long periods on stream. Therefore, catalyst support with high surface area is highly favourable. Many studies have been performed on Ni catalyst by varying catalyst supports, such as metal oxides (SiO_2, TiO_2, Al_2O_3, and MgO) and carbonaceous materials. The enhanced effects of these supports have been investigated [18–24].

Several works on Ni-based catalysts were discussed here. For example, Gac et al. [25] reported the effect of Ni crystallite size on the catalytic activity in methane decomposition by introducing MgO into Ni–Al_2O_3 catalyst. The decrease in Ni crystallite size was observed which favoured the methane decomposition. It could be associated with the strong metal–support interaction. The initial activity of Ni–Al_2O_3 is higher, and the deactivation occurs faster for Ni–MgO–Al_2O_3 catalyst than those of the MgO-rich catalyst

due to the structural changes in Ni crystallite with carbon deposition which caused the blockage on the active surface of the catalyst as the amount of carbon increased with the increment of MgO addition. Salipira et al. [26] studied the effect of Ni loading on TiO_2 support. The methane conversion of Ni/TiO_2 catalyst increases along with the increment of the Ni loading from 7 to 20% prepared by impregnation method. The results agreed with those of Pudukudy et al. [24], who used high amounts of Ni loading (10–50 wt%) and used a one-pot sol–gel method to prepare the catalyst. All catalysts displayed high stability during 360 min on stream with highest activity were achieved by 50 wt% Ni/TiO_2. The stability test was conducted over 50 wt% Ni/TiO_2 for 960 min, and no extreme deactivation was observed throughout the reaction. The activity decreased slowly due to the less contact of methane molecules towards the availability of active Ni particles after long reaction time.

In addition to transition metal oxide-based supports, the mesoporous silica-based materials, such as MCM-41, MCM-48, SBA-15, KIT-5, KIT-6 and zeolites have been used as catalyst supports in methane decomposition. These materials possess high surface area and unique surface features that improve the catalytic activity of methane decomposition by enhancing metal dispersion on the support and favour an improved metal support interaction [27]. Guevara et al. [28] examined the activity of Ce-modified Ni/MCM-41 catalyst in methane decomposition. The Ni/Ce-MCM-41 catalyst showed a high stability during 1400 min of reaction time without any evident deactivation. An outstanding stability of the catalyst with high conversion of methane (74%) at 580 °C could be attributed to the synergy of Ce with Ni/MCM-41. Meanwhile, Pudukudy et al. [29] evaluated the activity of Ni-based catalyst over SBA-15 support. The catalytic performance of Ni/SBA-15 in terms of hydrogen yield is higher than that of Ni/$MgAl_2O_4$ [23] with considerable stability for 420 min on stream. The results agreed with those of Gómez et al. [30] and Urdiana et al. [31], who showed outstanding stability during 780 and 1440 min on stream, respectively due to the strong interaction between Ni and SBA-15 support caused by the hexagonal mesoporous structure of the support. The activity of Ni catalysts over the difference pore structure of mesoporous silica materials as catalyst support were examined by Tanggarnjanavalukul et al. [32]. Monomodal and bimodal porous materials with straight (SBA-15, MCM-41) and sinusoidal pores with the same and different pore sizes (Xerogel-5 and BPS-5) were used as catalyst supports over Ni catalyst and synthesized using incipient wetness impregnation method. The resulting kinetic activities of Ni-based catalysts followed the order of Ni/Xerogel-5 < Ni/SBA-15 < Ni/MCM-41 < Ni/BPS-5. The highest activity and stability in methane decomposition conducted at 500 °C were achieved by Ni/BPS-5 catalyst. Compared with MCM-41, SBA-15 and Xerogel-5, BPS-5

possesses the largest pore size which has a positive effect on the catalytic performance of Ni catalyst. Therefore, the properties of pore and its size influence the overall activity in methane decomposition in terms of allowing Ni particles to disperse well on the catalyst support [33].

A special type of mesoporous silica, namely mesostructured silica nanoparticle (MSN), is introduced in recent years with uniform pore distribution, tunable pore size, high chemical, mechanical and thermal stability and ordered porous network, thereby allowing a free and improved diffusion of the reactant substrate [34, 35]. The MSN is commonly used in catalysis as catalyst support and in drug delivery application [36–38]. MSNs are ideally suited for catalyst support due to its extremely high surface area (~ 1000 m^2/g), mesopores and the ability of MSN to promote the dispersion of metals on the surface of MSN. These characteristics of MSN may help in improving the dispersion of Ni particles on the surface of MSN, despite of different loadings of Ni [38]. This is because generally, high loading of Ni would lead to the aggregation of Ni particles thus producing larger particles in size, meanwhile, low loading of Ni would result in the high dispersion of Ni on the surface of support. Recent studies are focused on maximising hydrogen production and improving catalyst stability for long flow periods at the same time. In this paper, we report the use of MSN as a catalyst support for the application of Ni catalyst in methane decomposition. Considering the current studies on methane decomposition, to our knowledge, this is the first work that uses MSN as a catalyst support for methane decomposition, although other mesoporous silicas have been investigated widely, as discussed in detail above. The effect of Ni loading on the physicochemical properties and activity for methane decomposition is investigated. The MSN provided an improved metal dispersion in the catalyst and effectively favoured the reaction with increased methane conversion and catalyst stability.

2 Experimental

2.1 Synthesis of MSNs

A sol–gel method was used for MSN synthesis, as reported by Aziz et al. [36]. Firstly, 9.68 g cetyltrimethylammonium bromide (Merck), 58 ml of ammonia solution and 240 ml of ethylene glycol (Merck) were dissolved in 1440 ml of deionised water and then stirred at 50 °C for 30 min. Then, 11.4 ml of tetraethyl orthosilicate (Merck) and 2.1 ml of 3-(triethoxysilyl)-propylamine (Merck), which act as silica precursors were added slowly into the mixture, thereby turning the clear mixture into a white suspension. Then, the solution was further stirred at 80 °C for 2 h. Afterwards, the white solution was kept in a refrigerator for separation into two layers. After several days, the white precipitate separated in the solution was collected and washed several times with the distilled water and ethanol mixture ratio of 1:1. The obtained as-synthesized MSN was dried in the oven overnight at 110 °C and then calcined for 3 h at 550 °C.

2.2 Synthesis Ni/MSN catalysts

A wet impregnation method was used to synthesise the MSN supported Ni catalysts. The desired amount of Ni salt, Ni $(NO_3)_2 \cdot 6H_2O$ was weighed in accordance to 5, 10, 30 and 50 wt% Ni in the catalyst and dissolved in 500 ml of deionised water to become an aqueous nickel salt solution. Then, the catalyst support, MSN, was added delicately into the aqueous solution, and the solution was heated and mixed with magnetic stirrer at 90 °C until it became a homogenous paste. Afterwards, the obtained paste was dried in the oven overnight and finally calcined for 3 h at 550 °C. The resulting Ni/MSN catalyst was in the form of greyish powder and labelled as 5%, 10%, 30% and 50% Ni/MSN.

2.3 Characterization of the fresh and spent catalysts

The physicochemical properties of the fresh catalysts were examined by various methods. X-Ray diffraction (XRD) analysis was used to determine the phase and crystalline structure of the catalysts by using a D8 Advance (Bruker) instrument. The Cu Kα monochromatic radiation with a wavelength of 1.5406 Å was used to record the XRD patterns. The diffraction angle was set from 0° to 80°, and Scherrer equation was used to calculate the crystallite size. The surface properties of the catalyst were characterized using Fourier transform infrared spectroscopy (FTIR) by using a NICOLET 6700 IR spectroscope (Thermo Scientific), and transmission mode was used to record the spectra in the 400–4000 cm^{-1} region. The BET/BJH method was carried out in a Micromeritics ASAP 2020 at − 196 °C to measure the N_2 adsorption–desorption isotherms, together with the pore size distribution and pore volume. The samples were firstly degassed for 6 h at 300 °C before starting the analysis. The reducibility of the catalysts was studied via the temperature-programmed reduction (TPR) analysis by using Thermo Finnigan TPDRO 1100 model. The analysis was performed from 50 to 950 °C under 5% H_2 in Ar gas mixture with the flow rate of 30 ml/min and a heating rate of 10 °C/min. A gas chromatograph (GC) equipped with a thermal conductivity detector (TCD) was connected to the TPR instrument and used to analyse the total hydrogen consumed by each catalyst. The surface morphology of the catalysts was studied using field emission scanning electron microscope (FESEM) conducted in Zeiss MERLIN COMPACT machine with an accelerating voltage of 3 kV. The

crystalline features of the deposited carbon were analysed by XRD and Raman spectroscopy (Thermo Scientific DXR2xi model), and the internal morphology of the deposited carbon was examined by FESEM and transmission electron microscope (TEM; Thermo Fisher, Talos 120C model).

2.4 Catalytic testing for methane decomposition

The catalytic performances of the catalysts in methane decomposition were tested in a tubular fixed-bed reactor made of stainless steel (height of 60 cm, inner diameter of 2.5 cm) that was heated in an electric muffle. The reaction was performed at a fixed temperature (700 °C) under atmospheric pressure. The catalyst was packed in the middle of the reactor with the desired weight of the catalyst (i.e. 1.0 g). The treatment began with the reduction of the catalyst with a hydrogen flow rate of 150 ml/min at 600 °C for 90 min. Afterwards, the treatment was continued by N_2 gas with a flow rate of 150 ml/min to increase the temperature of the reactor up to 700 °C. The catalytic testing was carried out with an undiluted methane flow rate of 150 ml/min for 360 min of reaction under atmospheric pressure (0.1 MPa). The outlet gases were collected in the gas bags, and a GC 2014C (Shimadzu) equipped with TDX-01 column that was connected to TCD was used to analyse the outlet products with He as the carrier gas. After the completion of the reaction for 360 min, N_2 gas was flowed out into the reactor for cooling purposes, with the flow rate of 50 ml/min. The spent catalyst in the form of solid carbon was collected and taken for analysis. The hydrogen yield was calculated using the method reported by Pinilla et al. [39], whereas the carbon yield was calculated from the amount of catalyst used initially and the amount of carbon deposited after 360 min of methane decomposition [40].

3 Results and discussion

3.1 Characterization of the Ni/MSN catalysts

The XRD patterns of all of the synthesized catalysts are shown in Fig. 1. Figure 1a presents the small-angle XRD patterns of the MSN support and Ni/MSN catalysts. It displays three significant peaks at the 2θ values of 2.2°, 3.9° and 4.5°, and these peaks were assigned to (100), (110) and (200) planes, respectively, which can be attributed to the characteristic features of mesoporous silica [36, 37, 41]. The existence of high-order peaks, such as (110) and (200), indicates the high degree of ordered hexagonal pores in the materials [36]. The presence of metal species in the pores and surface of MSN and a degradation on the MSN framework decreased the intensity of the low-angle diffraction peaks with an increased Ni loading in the catalysts [36, 38].
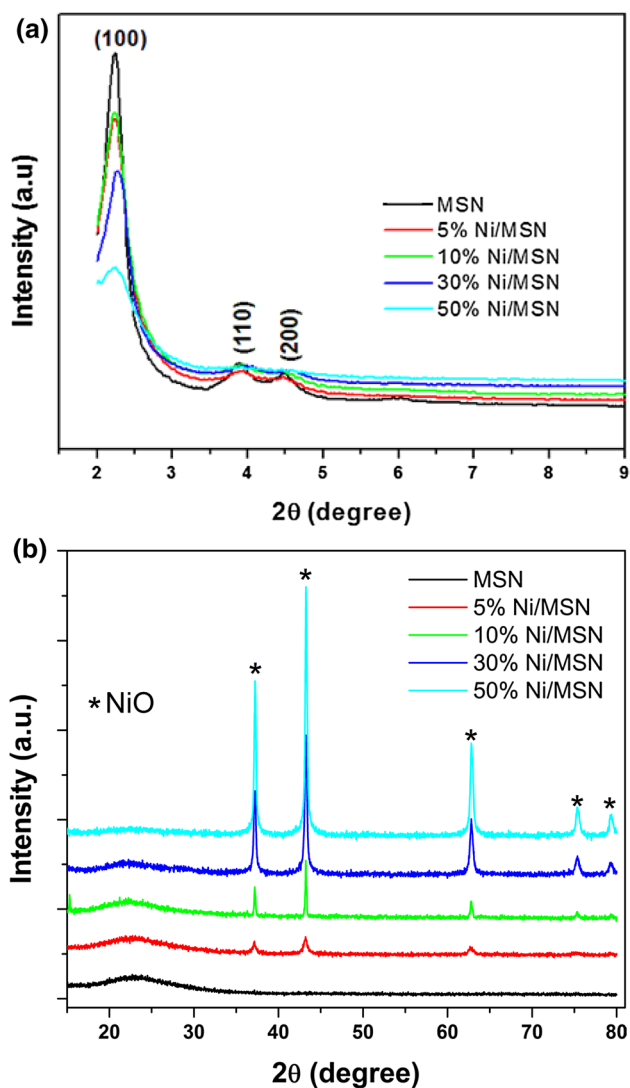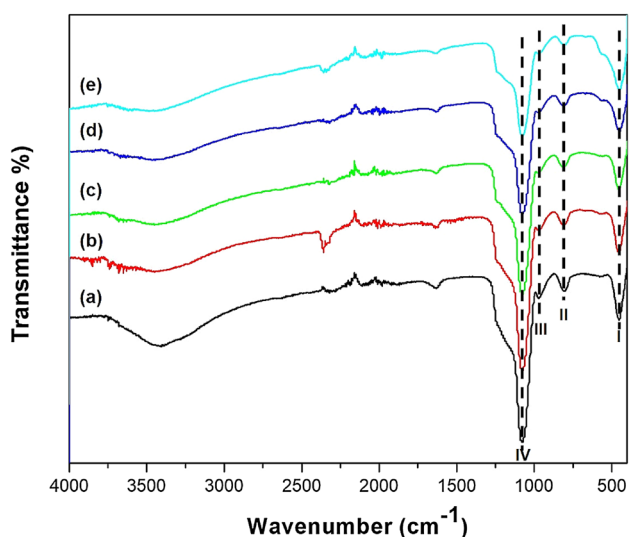

Fig. 1 XRD patterns of the prepared samples: **a** small and **b** wide angle diffraction patterns

In the XRD pattern of MSN in Fig. 1b, no diffraction peaks were detected. Meanwhile, only a weak hump was observed in the 2θ region of 20°–25°. This hump demonstrated the amorphous nature of MSN [37]. Nevertheless, several intense peaks were detected in all Ni/MSN catalysts with different Ni loadings. The peaks were located at 37.2°, 43.2°, 62.7°, 75.4° and 79.1° which belong to the face-centred, cubic-phase crystalline structure of NiO [40]. No other peaks were observed in the sample, thereby indicating the absence of impurities in the as-synthesized catalysts. The intensity of the peaks increased as the Ni loading increased. It could be due to the increased Ni amount in the catalyst, along with their increased crystallinity. The full width at half maximum of the intense peak were used to calculate the NiO crystallite size and the crystallite size which were calculated to be 9.5, 23.2, 28.6 and 39.4 nm for 5, 10, 30 and 50

wt% Ni/MSN catalysts, respectively. This result showed an increase in NiO crystallite size in the increased Ni amount in the catalysts, thereby indicating the enhanced crystallinity of NiO over MSN. Moreover, MSN can allow the metal species to be properly dispersed on the MSN surface.

Figure 2 shows the FTIR spectra of the MSN and Ni/MSN catalysts. The presence of an intense band at 1077 cm^{-1} (peak IV) was assigned to the asymmetric stretching vibration of Si–O–Si bridges, and other bands at 806 cm^{-1} (peak II) and 454 cm^{-1} (peak I) were ascribed to the symmetric and asymmetric stretching vibrations of the Si–O bonds. The presence of these peaks confirmed the MSN formation [37]. The weak band at 967 cm^{-1} (peak III) was detected corresponding to the stretching vibration of Si–OH of the surface silanol groups. It might be also induced by the presence of transition metal atoms that are close to the silica framework because the stretching vibration mode of Si–O is interrupted by the adjacent metal ions [41]. The transmission bands related to Ni–O bonds in the region of 450 cm^{-1} can be merge with the SiO_2 peaks [41, 42]. Nevertheless, no band shift was observed for MSN after metal deposition, thereby indicating that the Ni particles did not interfere the MSN framework. The broad band at 3431 cm^{-1} was assigned to the stretching and bending vibrations of the O–H group which were initiated by the existence of adsorbed water molecules.

Figure 3 displays the FESEM images of the MSN support and Ni/MSN catalysts with different Ni loading. As shown in Fig. 3a, the highly uniform spherical particles with 10–20 nm size were observed for the MSN support. However, there is no severe difference in the surface morphology was observed for the catalysts with low Ni loadings, as

shown in Fig. 3b–d. However, the increased in Ni loading, such as 50%, resulted in the formation of large particles with the size varying from 30 to 60 nm, as shown in Fig. 3e. However, the particle aggregation is somewhat similar in all of the catalysts. It further validates that the growth of NiO particles over MSN was regulated in the present set of catalysts. Figure 4 shows the FESEM mapping analysis of the catalysts. All catalysts displayed the effective dispersion of Ni species on the surface of MSN, in agreement with TEM images of the Ni loaded catalysts as shown in Fig. 5. In general, high loading of Ni would lead to the aggregation of Ni particles thus producing larger particles in size, meanwhile, low loading of Ni would result in the high dispersion of Ni on the surface of support [43]. The TEM images show the presence of well-resolved pores in the MSN support, and the NiO particles were dispersed on the MSN surface.

The textural properties of the synthesized catalysts were examined using BET/BJH analysis, and the results of the surface area and porosity are shown in Table 1. An extremely high surface area of 1094.8 m^2/g belonged to MSN, with the mean pore size of 4.9 nm. However, the surface area of the MSN slightly dropped to 1007.7 m^2/g after 5% of Ni loading due to the blocking of NiO nanoparticles on MSN surface pore [44]. The Ni/MSN surface area continued to decrease, as shown in Table 1. The N_2-sorption isotherms of all catalysts shown in Fig. 6a indicated type IV isotherm which confirmed the mesoporous nature of the catalyst and hysteresis loop H4 which illustrates the narrow slit-like pores together with particles of irregular inner voids [37]. The decrease in the surface area of the catalyst as the Ni loading increased indicating the pore blockage by the Ni species. The pore size distribution of all catalyst is presented in Fig. 6b. The pore size distribution of all catalyst was found to be in the range of 2.3–2.9 nm. All catalysts, including the MSN support, displayed an approximately equal pore size, whilst the pore volume decreased after Ni loading due to pore filling and/ or blocking with metal species. The pore volume of MSN continued to decrease with the addition of Ni.

TPR analysis was conducted to study the reducibility of the catalysts and metal support interactions in the catalysts. Figure 7 shows the TPR profiles for MSN and Ni/MSN catalysts with varying Ni loading. No reduction peaks were observed for MSN. All Ni/MSN catalysts displayed two main reduction peaks, as follows. The first main peak that is located at nearly 425 °C could be ascribed to the reduction of surface NiO particles having weak interaction with the MSN support [29]. The next peak observed at 550 °C can be related to NiO reduction with strong metal support interaction. These particles were expected to exist in the pores of MSN by metal trapping process and which are relatively difficult to reduce than the surface NiO particles. The second reduction peak of 30% and 50% Ni/MSN catalysts related to the reduction of strongly interacted NiO displayed a different

Fig. 2 FTIR spectra of the samples: (a) MSN and (b) 5%, (c) 10%, (d) 30% and (e) 50% Ni loaded catalysts

Fig. 3 FESEM images the **a** MSN and **b** 5%, **c** 10%, **d** 30% and **e** 50% Ni loaded catalysts
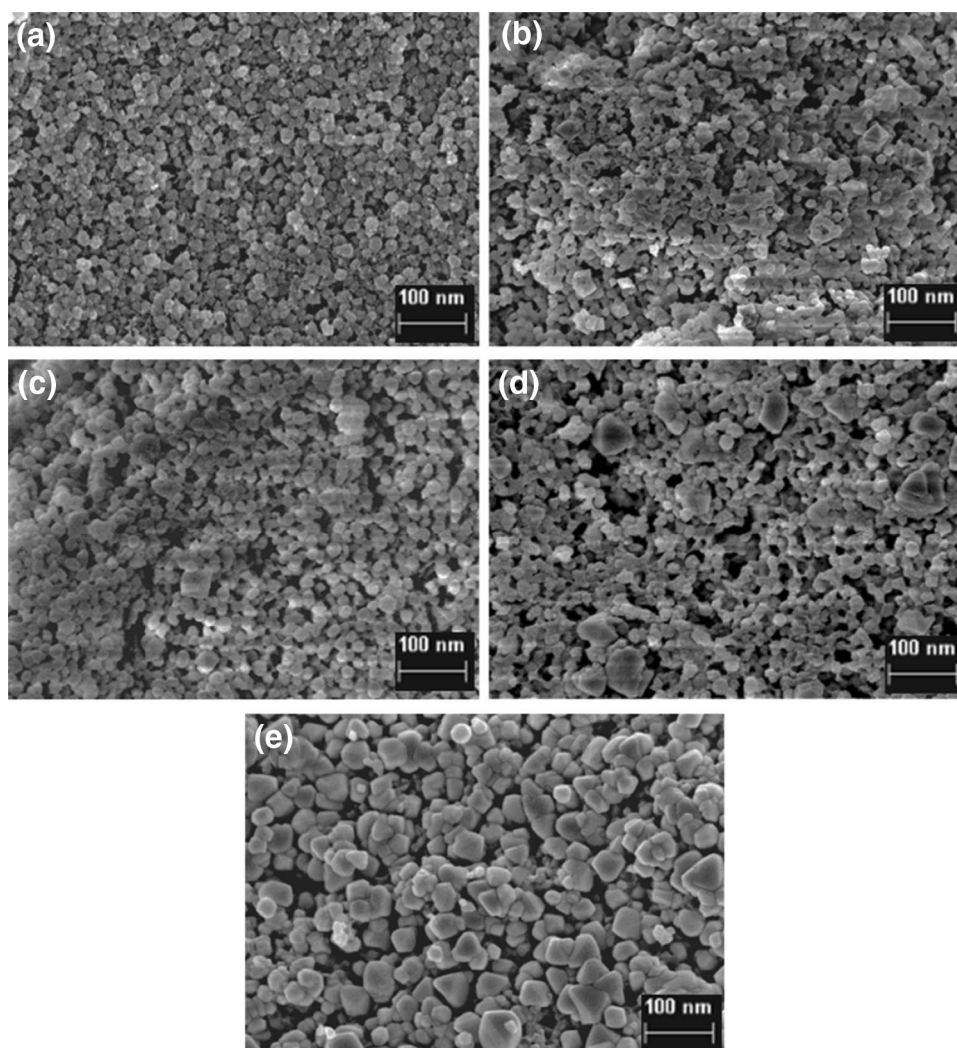

degree of interaction with MSN support [44]. The reduction peak positions were almost the same in all catalysts which further indicated the enhanced role of MSN for metal dispersion, which is consistent with the characterization results. The peak reduction area of 30% Ni/MSN was quite lower that compared to the 10% Ni/MSN as shown in Fig. 7. It might be associated with the high interaction of NiO species with the MSN support which lead to the production of more encapsulating NiO on the MSN pores, resulting in the weak reducibility of NiO species as reported previously [29]. It is quite deviated from the expected results that the increased nickel loading could result in the high reduction peak area due to increased consumption of hydrogen for the reduction of metal oxide.

3.2 Catalytic activity for methane decomposition

Methane decomposition was performed using Ni/MSN catalysts with varying Ni loadings to study the effect of Ni loading on their catalytic activity. The metal loading

reported in this work is based on previous research results [24, 45, 46]. As Ni/MSN is a metal-based catalyst, the loading of metal is very important. The higher loading of metal usually restricts the enhanced role of catalyst support such as MSN in the catalytic reaction. Therefore, we had selected the lower loading of metals with a maximum of 50%. Above 50%, the role of MSN could be diminished and the catalyst will be expected to shows the behaviours of unsupported catalyst. The reactions were conducted at 700 °C and atmospheric pressure condition with 150 ml/min flow of methane gas. The kinetic curves of the methane decomposition are shown in the Fig. 8. All catalysts exhibited high hydrogen yield in the first few minutes on the stream. After 20 min of reaction, a Ni amount dependent activity was observed. The hydrogen yield reached 51%, 57%, 54% and 62% for 5%, 10%. 30% and 50% Ni loaded catalysts, respectively. However, a rapid decrease in hydrogen yield was observed for 5% Ni/MSN catalyst after 30 min of reaction. The yield significantly decreased to 14% and continued for the entire reaction. This result

Fig. 4 FESEM elemental mapping results of the prepared samples
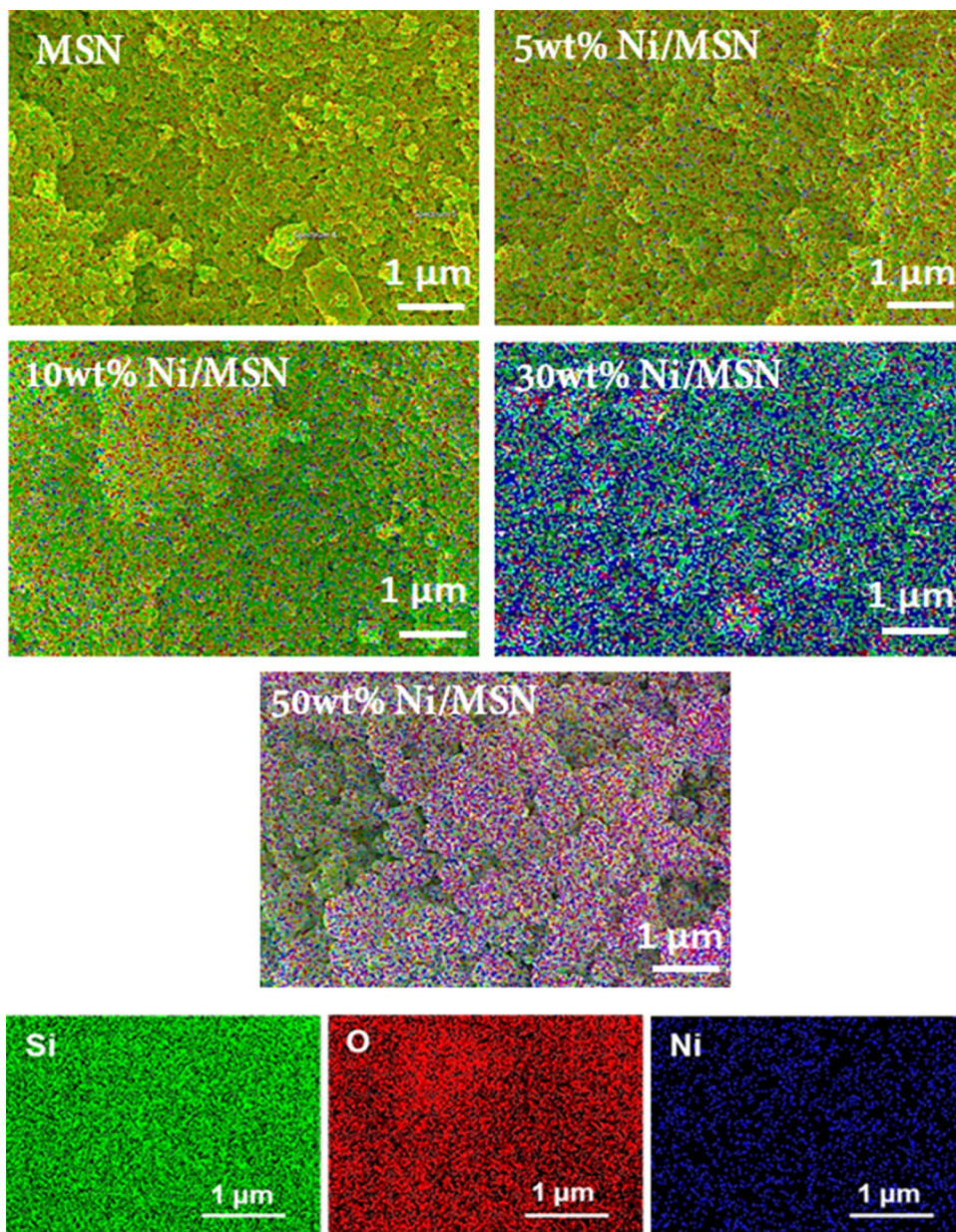
can be associated with the low Ni quantity in the catalyst. The same trend was observed for 10% Ni/MSN catalyst without an extreme decrease in the activity, in contrast to the 5% Ni/MSN catalyst, thereby indicating that the catalyst with 10% Ni loading was more stable than those with low Ni loading. A small increase in the hydrogen yield was observed for 30% Ni/MSN catalyst compared to 10% Ni/ MSN catalyst after 90 min of reaction. The activity continued more or less the same until end of reaction with 45% of hydrogen yield. Finally, 50% Ni/MSN catalyst showed the highest activity with maximum hydrogen yield of 68% and high stability in the entire reaction. No major deactivation was observed after 360 min on stream. The activity of Ni-based catalyst in methane decomposition as described

in the literature has been summarized in Table 2. The catalytic activity of 50% Ni/MSN catalyst was comparable with that of Ni catalyst that was supported over MCM-41, as described by Guevara et al. [28] although they used Ce as the promoter. The physicochemical properties of MSN play a crucial role in the improved activity and stability of Ni-based catalyst in methane decomposition. The homogeneous dispersion of metallic species on the MSN support with high surface area and a proper metal support interaction, as illustrated in the characterization results have contributed to the outstanding results in the activities and stability of the catalysts with high Ni loading [47]. The porous structure of MSN was maintained even though high loading of Ni was loaded on the MSN. Thus, MSN

Fig. 5 TEM images of the **a** MSN and **b** 5%, **c** 10%, **d** 30% and **e** 50% Ni loaded catalysts
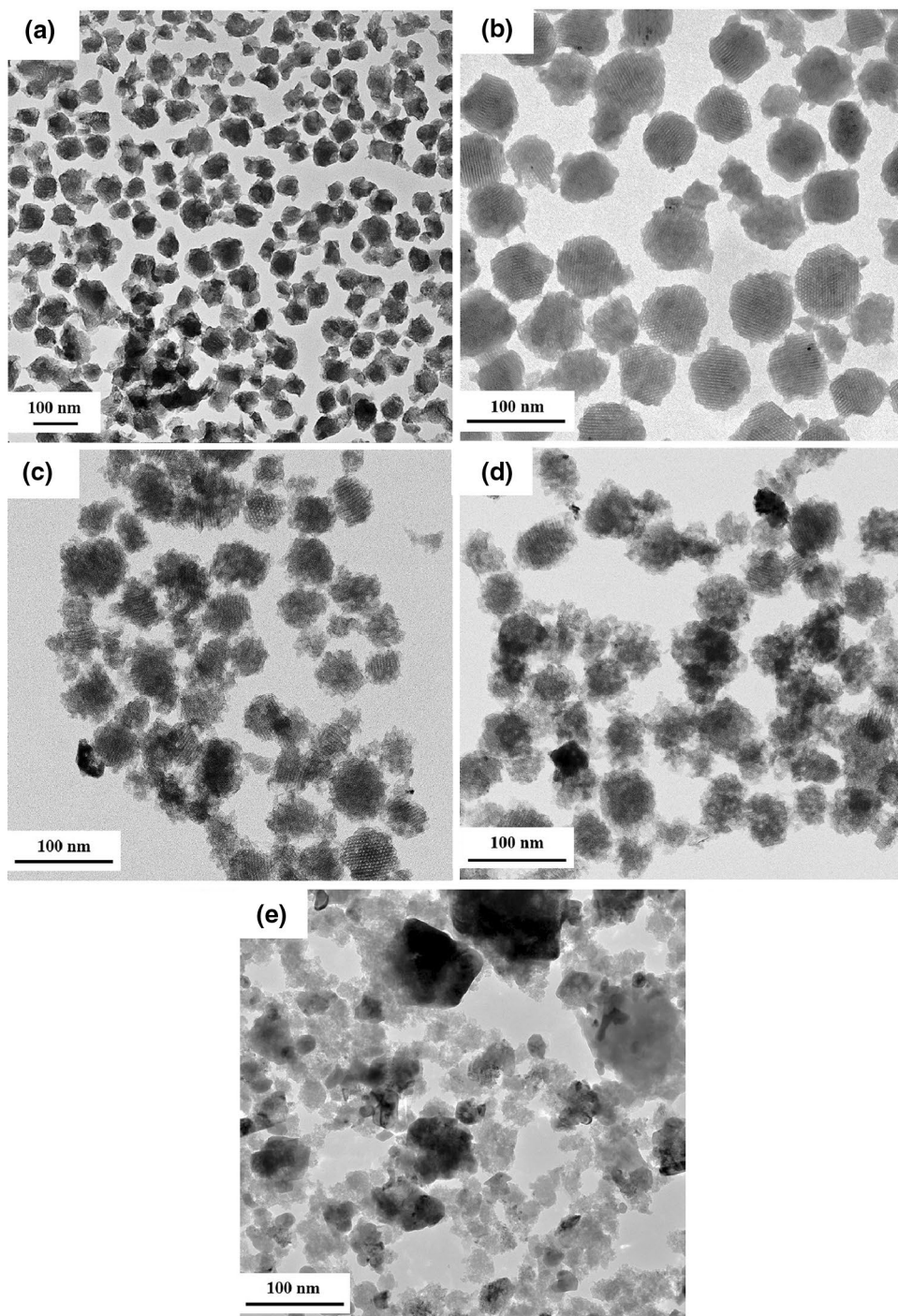
is a potential catalyst support in methane decomposition because it provides high catalytic activity and stability.

3.3 Spent catalyst characterization

The yield of deposited carbon was further calculated and it was found to be 129 wt%, 215 wt% 458 wt% and 906 wt% for the 5%, 10%, 30% and 50% Ni/MSN catalysts respectively. The carbon yield was found to be increased with the

increased loading of Ni in the catalyst and followed the same trend of their catalytic performance as shown in Fig. 8. The structural and crystalline properties of the spent catalyst were further characterized. Figure 9a displays the XRD patterns of the carbon obtained over Ni/MSN catalyst with different Ni loadings. The highest diffraction peak at 26.2° was assigned to the successful formation of crystalline carbon with (002) lattice plane, and another peak that was observed at 44.5° was also related to graphitic carbon [17]. Metallic

Table 1 BET/BJH results of the support and prepared catalysts obtained by N_2-physisorption analysis

Sample	BET surface area (m^2/g)	Mean pore size (nm)	Pore volume (cm^3/g)
MSN	1094.8	2.9	1.645
5% Ni/MSN	1007.7	2.6	1.250
10% Ni/MSN	933.0	2.6	1.235
30% Ni/MSN	682.0	2.5	0.902
50% Ni/MSN	409.4	2.3	0.514
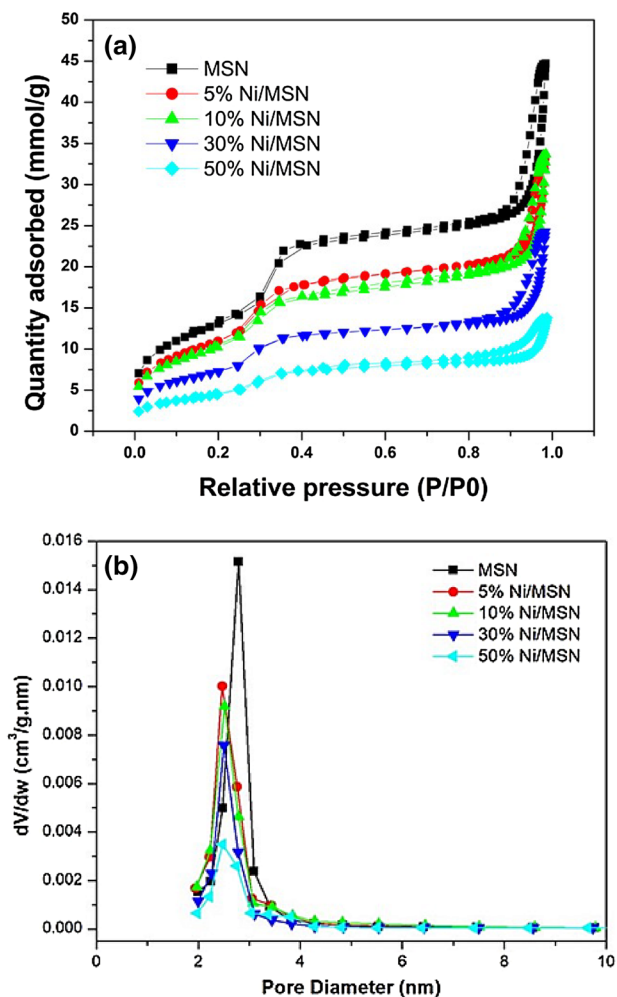
Fig. 6 **a** N_2 sorption isotherms and **b** pore size distribution plots of the MSN and Ni/MSN catalysts

Fig. 7 TPR profiles of the nickel loaded MSN catalysts
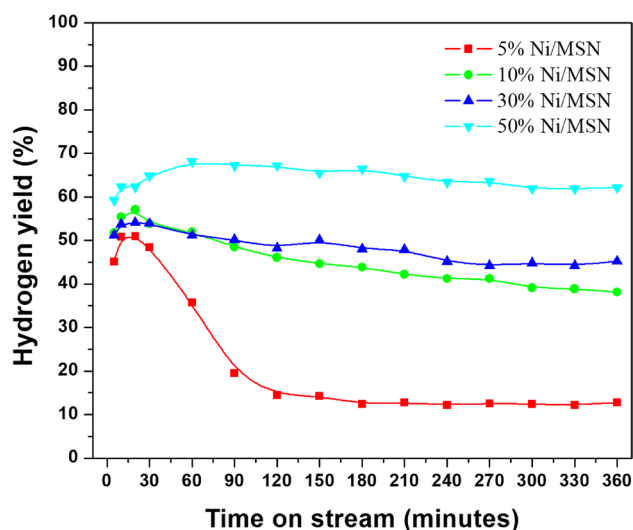
Fig. 8 Catalytic activity of the Ni/MSN catalysts for methane decomposition at 700 °C

Ni was also detected in the spent catalysts. Metallic Ni formation was caused by the NiO reduction during reduction or reaction, whereas the other peaks can be related to quartz wool used for catalyst packing. The higher the intensity of the peak is, the higher will be the crystallinity and graphitization degree of the carbon produced. This result further confirmed the bulk deposition of carbon nanomaterials. The interlayer distances of the deposited carbon were found be 0.337 nm, 0.336 nm, 0.336 nm and 0.337 nm for 5%, 10%, 30% and 50% Ni/MSN catalysts, respectively. These values are close to the ideal value of 0.335 nm, thereby reflecting the high crystalline quality of carbon. The carbon peak intensity also increased with the increased amount of Ni in the catalysts. It could be due to the high carbon deposition. However, the well-dispersed Ni nanoparticles on the surface of the MSN support is responsible for the high stability of the Ni/MSN catalysts.

Figure 9b shows the Raman spectra of the deposited carbon over Ni/MSN catalysts with different Ni loadings. Two well-defined bands were observed in each sample and which are centred at 1342 cm^{-1} and 1582 cm^{-1}. The first band

Table 2 Comparison of the activity of Ni-based catalysts for methane decomposition

Catalyst	BET surface area (m²/g)	Mean pore size (nm)	Methane conversion (%)	Hydrogen yield (%)	Ref.
Ni/MgAl$_2$O$_4$	22.6	23.6	–	49	[23]
Ni/Al$_2$O$_3$	69.1	–	48	–	[25]
Ni/MgO–Al$_2$O$_3$	95.4	–	13	–	[25]
Ni/TiO$_2$	40.2	–	71	–	[26]
Ni/TiO$_2$	12.31	31.3	–	55	[24]
Ni/SBA-15	182.6	5.9	–	52	[29]
Ni/SBA-15	339.0	4.9	40	–	[31]
Ni/SBA-15	552.0	6.5	74	–	[32]
Ni/Xerogel-5	481.0	6.5	60	–	[32]
Ni/MCM-41	947.0	12.7	68	–	[32]
Ni/Ce-MCM-41	–	–	70		[28]
Ni/BPS-5	436.0	41.7	78	–	[32]
Ni/MSN	409.4	2.3	–	68	This work
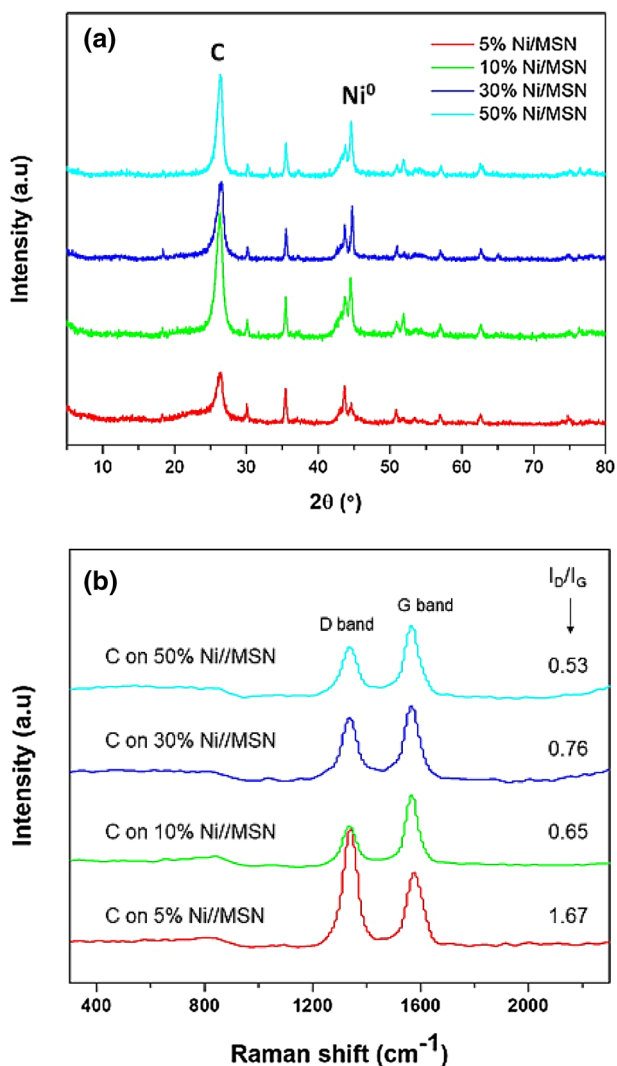
Fig. 9 a XRD patterns and **b** Raman spectra of the spent catalysts

was related to the D band, which is assigned to the structural defects in the graphitic carbon. Meanwhile, the second band was assigned to the G band, which is associated to the stretching vibration of the in-plane C–C bonds [48, 49]. The I_D/I_G ratio was used to evaluate the crystallinity and graphitization degree of the nanocarbon produced [50]. The I_D/I_G ratios were calculated to be 1.67, 0.53, 0.76 and 0.65 for 5%, 10%, 30% and 50% Ni/MSN catalysts, respectively. The carbon deposited over the 5% sample showed high I_D/I_G ratio, indicating its lower graphitization degree than those of the other samples. The low I_D/I_G ratio indicates the high crystallinity and graphitization degree of the deposited carbon [24, 49, 51]. The high I_D/I_G ratio is correlated to the growth of disordered carbon over the catalysts [52, 53].

The morphology of carbon-deposited catalyst was analysed by using FESEM and TEM analyses and the results are illustrated in Figs. 10 and 11, respectively. As shown in the FESEM images, the bulk deposition of the nanocarbon in tubular forms with the diameter range of 20–45 nm was observed over 50% Ni/MSN catalyst. The TEM images shown in Fig. 11 confirmed the formation of multiwalled carbon nanotubes over the prepared catalysts with an average diameter range of 25–35 nm, regardless of the Ni content in the catalysts. The hollow channel of the carbon nanotubes is highly visible in the samples.

4 Conclusions

The catalytic performance of the Ni/MSN catalysts with different Ni loadings such as 5%, 10%, 30% and 50%, that were synthesized by an impregnation method was investigated for undiluted methane decomposition. The characterization results demonstrated that the porous structure of MSN is well preserved in the prepared catalysts even after the

Fig. 10 FESEM images of the carbon nanotubes deposited over 50% Ni/MSN catalyst
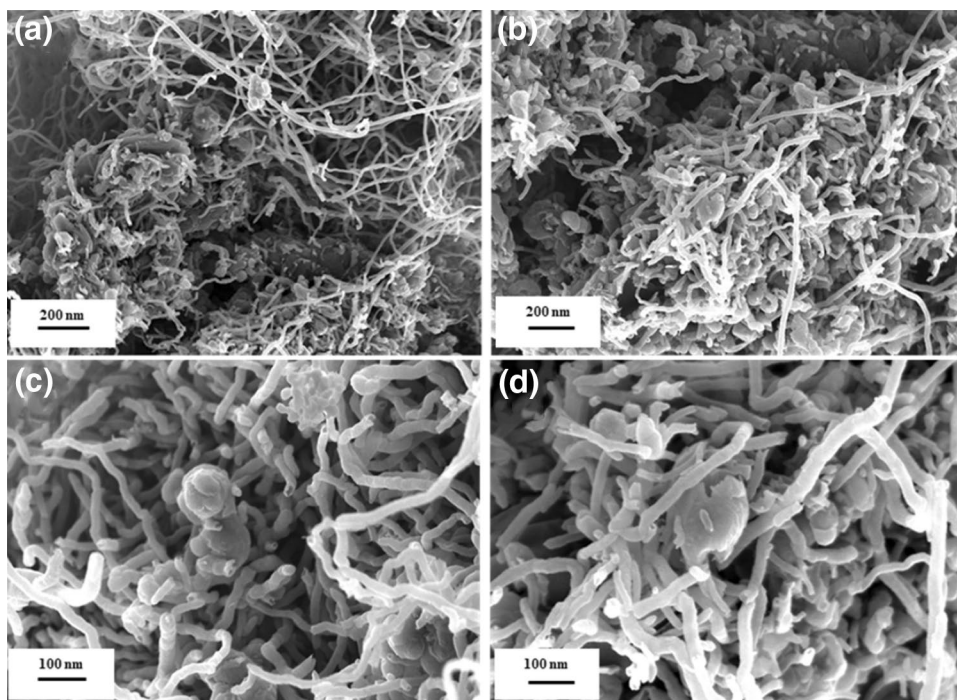
Fig. 11 TEM images of the CNTs deposited over **a** 5%, **b** 10%, **c** 30% and **d** 50% Ni/MSN catalysts
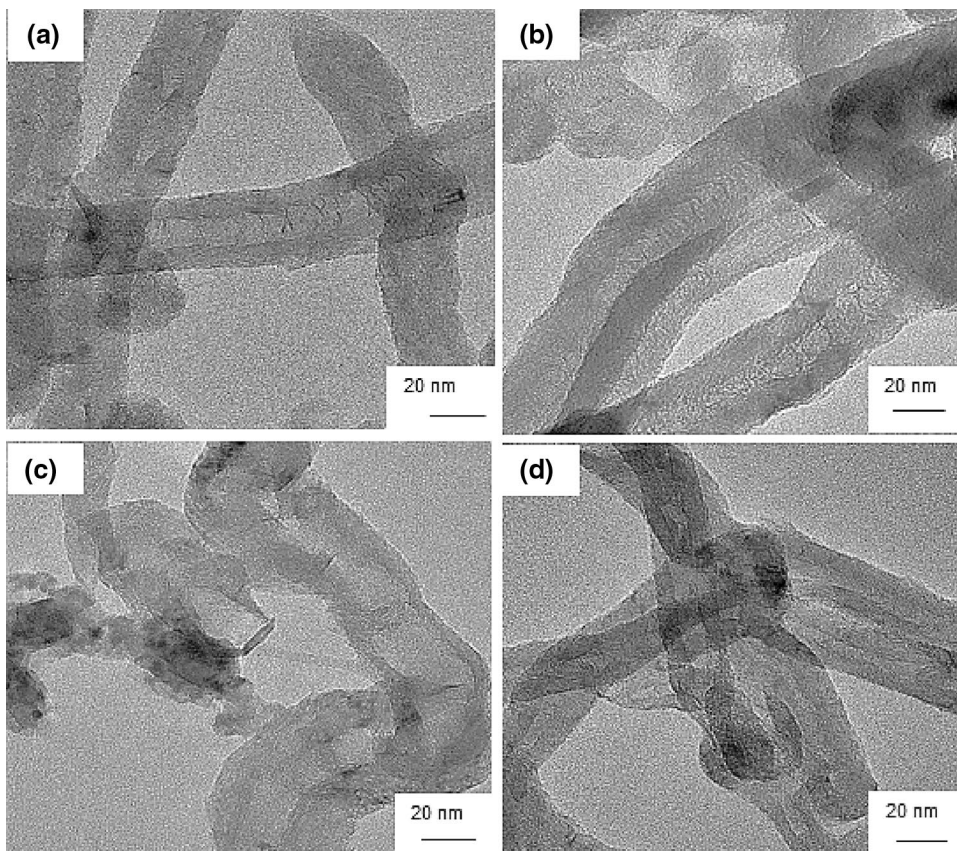
incorporation of high Ni amounts. The active phase of nickel was found to be NiO in the fresh samples that were well dispersed on the surface of the MSN support with proper metal support interaction. The pore blocking of MSN by NiO species on the surface of MSN decreased the surface area of Ni/MSN catalysts, with increased Ni loading. The catalytic

activity tests revealed that the 50% Ni/MSN displayed the highest hydrogen yield of 68% with improved stability for 360 min of reaction. The pronounced catalytic performance of the catalyst could be assigned to the improved synergistic effects of nickel species with MSN support. The contributions of high surface area, dispersion of metal species on the support, an appropriate metal support interaction and the presence of metallic Ni nanoparticles are responsible for the high catalytic efficiency of the Ni/MSN catalysts. The characterization studies of the deposited carbon showed that multiwalled carbon nanotubes with high crystallinity and graphitization degree were formed over Ni/MSN catalysts after decomposition reaction.

Compliance with ethical standards

Conflict of interest The authors declare that they have no conflict of interest.

References

1. P. Hoffmann, *Tomorrow's Energy: Hydrogen, Fuel Cells and the Prospects for a Cleaner Planet* (The MIT Press, London, 2012)
2. P. Kruger, *Alternative Energy Resources: The Quest for Sustainable Energy* (Wiley, Hoboken, 2006)
3. A. Kumar, J.P. Chakraborty, R. Singh, Bio-oil: the future of hydrogen generation. Biofuels (2016). https://doi.org/10.1080/17597269.2016.1141276
4. P. Mierczynski, K. Vasilev, A. Mierczynska, W. Maniukiewicz, R. Ciesielski, J. Rogowski, I.M. Szynkowska, A.Y. Trifonov, S.V. Dubkov, D.G. Gromov, T.P. Maniecki, The effect of gold on modern bimetallic Au–Cu/MWCNT catalysts for the oxy-steam reforming of methanol. Catal. Sci. Technol. **6**, 4168–4183 (2016). https://doi.org/10.1039/C5CY01667C
5. N.D. Subramanian, J. Callison, C.R.A. Catlow, P.P. Wells, N. Dimitratos, Optimised hydrogen production by aqueous phase reforming of glycerol on Pt/Al$_2$O$_3$. Int. J. Hydrog. Energy **1**, 1–10 (2016). https://doi.org/10.1016/j.ijhydene.2016.08.081
6. Y. Jiao, J. Zhang, Y. Du, F. Li, C. Li, J. Lu, J. Wang, Y. Chen, Hydrogen production by catalytic steam reforming of hydrocarbon fuels over Ni/Ce–Al$_2$O$_3$ bifunctional catalysts: effects of SrO addition. Int. J. Hydrog. Energy **41**, 13436–13447 (2016). https://doi.org/10.1016/j.ijhydene.2016.05.178
7. A.L. Alberton, M.M.V.M. Souza, M. Schmal, Carbon formation and its influence on ethanol steam reforming over Ni/Al$_2$O$_3$ catalysts. Catal. Today **123**, 257–264 (2007). https://doi.org/10.1016/j.cattod.2007.01.062
8. K. Takeishi, Y. Akaike, Hydrogen production by dimethyl ether steam reforming over copper alumina catalysts prepared using the sol–gel method. Appl. Catal. A Gen. **510**, 20–26 (2016). https://doi.org/10.1016/j.apcata.2015.09.027
9. K.K. Pant, R. Jain, S. Jain, Renewable hydrogen production by steam reforming of glycerol over Ni/CeO$_2$ catalyst prepared by precipitation deposition method. Korean J. Chem. Eng. **28**, 1859–1866 (2011). https://doi.org/10.1007/s11814-011-0059-8
10. E. Gallegos-Suárez, A. Guerrero-Ruiz, I. Rodríguez-Ramos, Efficient hydrogen production from glycerol by steam reforming with carbon supported ruthenium catalysts. Carbon **96**, 578–587 (2016). https://doi.org/10.1016/j.carbon.2015.09.112
11. K.C. Mondal, S.R. Chandran, Evaluation of the economic impact of hydrogen production by methane decomposition with steam reforming of methane process. Int. J. Energy Res. **39**, 2–6 (2014). https://doi.org/10.1016/j.ijhydene.2014.04.087
12. S. Li, M. Li, C. Zhang, S. Wang, X. Ma, J. Gong, Steam reforming of ethanol over Ni/ZrO$_2$ catalysts: effect of support on product distribution. Int. J. Hydrogen Energy **37**, 2940–2949 (2012). https://doi.org/10.1016/j.ijhydene.2011.01.009
13. X. Zhang, A. Kätelhön, G. Sorda, M. Helmin, M. Rose, A. Bardow, M. Reinhard, R. Palkovits, A. Mitsos, CO$_2$ mitigation costs of catalytic methane decomposition. Energy **151**, 826–838 (2018). https://doi.org/10.1016/j.energy.2018.03.132
14. K. Srilatha, D. Bhagawan, S.S. Kumar, V. Himabindu, Sustainable fuel production by thermocatalytic decomposition of methane–a review. S. Afr. J. Chem. Eng. (2017). https://doi.org/10.1016/j.sajce.2017.10.002
15. A.S. Al-Fatesh, A.H. Fakeeha, W.U. Khan, A.A. Ibrahim, S. He, K. Seshan, Production of hydrogen by catalytic methane decomposition over alumina supported mono-, bi- and tri-metallic catalysts. Int. J. Hydrog. Energy **41**, 22932–22940 (2016). https://doi.org/10.1016/j.ijhydene.2016.09.027
16. J. Majewska, B. Michalkiewicz, Production of hydrogen and carbon nanomaterials from methane using Co/ZSM-5 catalyst. Int. J. Hydrog. Energy. **41**, 8668–8678 (2016). https://doi.org/10.1016/j.ijhydene.2016.01.097
17. A. Rastegarpanah, F. Meshkani, M. Rezaei, Thermocatalytic decomposition of methane over mesoporous nanocrystalline promoted Ni/MgO·Al$_2$O$_3$ catalysts. Int. J. Hydrog. Energy **42**, 16476–16488 (2017). https://doi.org/10.1016/j.ijhydene.2017.05.044
18. G.D.B. Nuernberg, E.L. Foletto, C.E.M. Campos, H.V. Fajardo, N.L.V. Carre, Direct decomposition of methane over Ni catalyst supported in magnesium aluminate. J. Power Sources **208**, 409–414 (2012). https://doi.org/10.1016/j.jpowsour.2012.02.037
19. J. Li, Y. Gong, C. Chen, J. Hou, L. Yue, X. Fu, L. Zhao, H. Chen, H. Wang, S. Peng, Evolution of the Ni-Cu-SiO$_2$ catalyst for methane decomposition to prepare hydrogen. Fusion Eng. Des. (2017). https://doi.org/10.1016/j.fusengdes.2017.05.040
20. Z. Bai, H. Chen, B. Li, W. Li, Methane decomposition over Ni loaded activated carbon for hydrogen production and the formation of filamentous carbon. Int. J. Hydrog. Energy **32**, 32–37 (2007). https://doi.org/10.1016/j.ijhydene.2006.06.030
21. A.E. Awadallah, S.M. Solyman, A.A. Aboul-Enein, H.A. Ahmed, N.A.K. Aboul-Gheit, S.A. Hassan, Effect of combining Al, Mg, Ce or La oxides to extracted rice husk nanosilica on the catalytic performance of NiO during COx-free hydrogen production via methane decomposition. Int. J. Hydrog. Energy (2017). https://doi.org/10.1016/j.ijhydene.2017.03.049
22. I. Abdullahi, N. Sakulchaicharoen, J.E. Herrera, A mechanistic study on the growth of multi-walled carbon nanotubes by methane decomposition over nickel-alumina catalyst. Diam. Relat. Mater. **23**, 76–82 (2012). https://doi.org/10.1016/j.diamond.2012.01.017
23. M. Pudukudy, Z. Yaakob, M.S. Takriff, Methane decomposition over Pd promoted Ni/MgAl$_2$O$_4$ catalyst for the production of COx free hydrogen and multiwalled carbon nanotubes. Appl. Surf. Sci. (2015). https://doi.org/10.1016/j.apsusc.2015.08.246

24. M. Pudukudy, Z. Yaakob, A. Kadier, M.S. Takriff, N.S. Mat Hassan, One-pot sol-gel synthesis of Ni/TiO₂ catalysts for methane decomposition into COx free hydrogen and multiwalled carbon nanotubes. Int. J. Hydrog. Energy **1**, 1–19 (2017)

25. W. Gac, A. Denis, T. Borowiecki, L. Kepiński, Methane decomposition over Ni–MgO–Al₂O₃ catalysts. Appl. Catal. A Gen. **357**, 236–243 (2009). https://doi.org/10.1016/j.apcata.2009.01.029

26. K. Salipira, N.J. Coville, M.S. Scurrell, Carbon produced by the catalytic decomposition of methane on nickel: carbon yields and carbon structure as a function of catalyst properties. J. Nat. Gas Sci. Eng. **32**, 501–511 (2016). https://doi.org/10.1016/j.jngse.2016.04.027

27. R. Huirache-Acuña, R. Nava, C.L. Peza-Ledesma, J. Lara-Romero, G. Alonso-Núñez, B. Pawelec, Rivera-Muñoz, SBA-15 mesoporous silica as catalytic support for hydrodesulfurization catalysts—review. Materials **6**, 4139–4167 (2013). https://doi.org/10.3390/ma6094139

28. J.C. Guevara, J.A. Wang, L.F. Chen, M.A. Valenzuela, P. Salas, A. García-Ruiz, J.A. Toledo, M.A. Cortes-Jácome, C. Angeles-Chavez, O. Novaro, Ni/Ce-MCM-41 mesostructured catalysts for simultaneous production of hydrogen and nanocarbon via methane decomposition. Int. J. Hydrog. Energy **35**, 3509–3521 (2010). https://doi.org/10.1016/j.ijhydene.2010.01.068

29. M. Pudukudy, Z. Yaakob, Z.S. Akmal, Direct decomposition of methane over Pd promoted Ni/SBA-15 catalyst. Appl. Surf. Sci. (2015). https://doi.org/10.1016/j.apsusc.2015.06.073

30. G. Gómez, J.A. Botas, D.P. Serrano, P. Pizarro, Hydrogen production by methane decomposition over pure silica SBA-15 materials. Catal. Today (2015). https://doi.org/10.1016/j.cattod.2015.12.007

31. G. Urdiana, R. Valdez, G. Lastra, M.A. Valenzuela, A. Olivas, Production of hydrogen and carbon nanomaterials using transition metal catalysts through methane decomposition. Mater. Lett. (2018). https://doi.org/10.1016/j.matlet.2018.01.033

32. C. Tanggarnjanavalukul, W. Donphai, T. Witoon, M. Chareonpanich, J. Limtrakul, Deactivation of nickel catalysts in methane cracking reaction: effect of bimodal meso-macropore structure of silica support. Chem. Eng. J. **262**, 364–371 (2015). https://doi.org/10.1016/j.cej.2014.09.112

33. Y. Lou, G. Toquer, S. Dourdain, C. Rey, C. Grygiel, D. Simeone, X. Deschanels, Structure evolution of mesoporous silica SBA-15 and MCM-41 under swift heavy ion irradiation. Nucl. Instrum. Methods Phys. Res. B. **365**, 336–341 (2015). https://doi.org/10.1016/j.nimb.2015.08.009

34. R.Y. Abrokwah, V.G. Deshmane, D. Kuila, Comparative performance of M-MCM-41 (M: Cu Co, Ni, Pd, Zn and Sn) catalysts for steam reforming of methanol. J. Mol. Catal. A: Chem. (2016). https://doi.org/10.1016/j.molcata.2016.09.019

35. O. Verho, F. Gao, E.V. Johnston, W. Wan, A. Nagendiran, H. Zheng, J.-E. Backvall, X. Zou, Mesoporous silica nanoparticles applied as a support for Pd and Au nanocatalysts in cycloisomerization reactions. APL Mater. (2014). https://doi.org/10.1063/1.4901293

36. M.A.A. Aziz, A.A. Jalil, S. Triwahyono, M.W.A. Saad, CO₂ methanation over Ni-promoted mesostructured silica nanoparticles: influence of Ni loading and water vapor on activity and response surface methodology studies. Chem. Eng. J. **260**, 757–764 (2015). https://doi.org/10.1016/j.cej.2014.09.031

37. S.M. Sidik, S. Triwahyono, A.A. Jalil, Z.A. Majid, N. Salamun, N.B. Talib, T.A.T. Abdullah, CO₂ reforming of CH₄ over Ni-Co/MSN for syngas production: role of Co as a binder and optimization using RSM. Chem. Eng. J. **295**, 1–10 (2016). https://doi.org/10.1016/j.cej.2016.03.041

38. S.M. Sidik, A. Abdul Jalil, S. Triwahyono, U.A. Asli, CO₂ reforming of methane over Ni supported on mesostructured silica nanoparticles (Ni/MSN) effect of Ni loading. J. Teknol. **78**, 13–18 (2016). https://doi.org/10.11113/jt.v78.9560

39. J.L. Pinilla, R. Utrilla, R.K. Karn, I. Suelves, M.J. Lázaro, R. Moliner, A.B. García, J.N. Rouzaud, High temperature iron-based catalysts for hydrogen and nanostructured carbon production by methane decomposition. Int. J. Hydrog. Energy. **36**, 7832–7843 (2011)

40. M. Pudukudy, A. Kadier, Z. Yaakob, M.S. Takriff, Non-oxidative thermocatalytic decomposition of methane into COx free hydrogen and nanocarbon over unsupported porous NiO and Fe₂O₃ catalysts. Int. J. Hydrog. Energy. (2016). https://doi.org/10.1016/j.ijhydene.2016.08.160

41. M.A.A. Aziz, A.A. Jalil, S. Triwahyono, S.M. Sidik, Methanation of carbon dioxide on metal-promoted mesostructured silica nanoparticles. Appl. Catal. A Gen. **486**, 115–122 (2014). https://doi.org/10.1016/j.apcata.2014.08.022

42. M. Pudukudy, Z. Yaakob, Methane decomposition over Ni, Co and Fe based monometallic catalysts supported on sol gel derived SiO₂ microflakes. Chem. Eng. J. **262**, 1009–1021 (2015). https://doi.org/10.1016/j.cej.2014.10.077

43. A.E. Awadallah, A.A. Aboul-Enein, A.K. Aboul-Gheit, Various nickel doping in commercial Ni–Mo/Al₂O₃ as catalyst for natural gas decomposition to COx–free hydrogen production. Renew. Energy **57**, 671–678 (2013). https://doi.org/10.1016/j.renene.2013.02.024

44. G. Naresh, V. Vijay Kumar, C. Anjaneyulu, J. Tardio, S.K. Bhargava, J. Patel, A. Venugopal, Nano size Hβ zeolite as an effective support for Ni and Ni-Cu for COx free hydrogen production by catalytic decomposition of methane. Int. J. Hydrog. Energy (2016). https://doi.org/10.1016/j.ijhydene.2016.09.131

45. J. Salmones, J.A. Wang, M.A. Valenzuela, E. Sánchez, A. Garcia, Pore geometry influence on the deactivation behavior of Ni-based catalysts for simultaneous production of hydrogen and nanocarbon. Catal. Today **148**, 134–139 (2009). https://doi.org/10.1016/j.cattod.2009.03.005

46. C. García-Sancho, R. Guil-López, L. Pascual, P. Maireles-Torres, R.M. Navarro, J.L.G. Fierro, Optimization of nickel loading of mixed oxide catalyst ex-hydrotalcite for H₂ production by methane decomposition. Appl. Catal. A Gen. (2017). https://doi.org/10.1016/j.apcata.2017.07.038

47. A.E. Awadallah, M.S. Mostafa, A.A. Aboul-Enein, S.A. Hanafi, Hydrogen production via methane decomposition over Al₂O₃–TiO₂ binary oxides supported Ni catalysts: effect of Ti content on the catalytic efficiency. Fuel **129**, 68–77 (2014). https://doi.org/10.1016/j.fuel.2014.03.047

48. M. Pudukudy, Z. Yaakob, M.Z. Mazuki, M.S. Takriff, S.S. Jahaya, One-pot sol-gel synthesis of MgO nanoparticles supported nickel and iron catalysts for undiluted methane decomposition into COx free hydrogen and nanocarbon. Appl. Catal. B Environ. **218**, 298–316 (2017). https://doi.org/10.1016/j.apcatb.2017.04.070

49. A.E. Awadallah, D.S. El-Desouki, N.A.K. Aboul-Gheit, A.H. Ibrahim, A.K. Aboul-Gheit, Effect of crystalline structure and pore geometry of silica based supported materials on the catalytic behavior of metallic nickel particles during methane decomposition to COx-free hydrogen and carbon nanomaterials. Int. J. Hydrog. Energy (2016). https://doi.org/10.1016/j.ijhydene.2016.07.081

50. M. Pudukudy, Z. Yaakob, Q. Jia, M.S. Takriff, Catalytic decomposition of methane over rare earth metal (Ce and La) oxides supported iron catalysts. Appl. Sur. Sci. **467–468**, 236–248 (2019). https://doi.org/10.1016/j.apsusc.2018.10.122

51. M. Pudukudy, Z. Yaakob, Q. Jia, M.S. Takriff, Catalytic decomposition of undiluted methane into hydrogen and carbon nanotubes over Pt promoted Ni/CeO₂ catalysts. New J. Chem. **42**, 14843–14856 (2018). https://doi.org/10.1039/c8nj02842g

52. A.E. Awadallah, A.A. Aboul-Enein, A.K. Aboul-Gheit, Effect of progressive Co loading on commercial Co–Mo/Al₂O₃ catalyst for natural gas decomposition to COx-free hydrogen production and

carbon nanotubes. Energy Convers. Manag. **77**, 143–151 (2014). https://doi.org/10.1016/j.enconman.2013.09.017

53. A.E. Awadallah, A.A. Aboul-Enein, D.S. El-Desouki, A.K. Aboul-Gheit, Catalytic thermal decomposition of methane to COx-free hydrogen and carbon nanotubes over MgO supported bimetallic group VIII catalysts. Appl. Sur. Sci. **296**, 100–107 (2014). https://doi.org/10.1016/j.apsusc.2014.01.055